Research Article Vol. 61, No. 17 / 10 June 2022 / Applied Optics 5049

applied optics

Nanostructured photosensitive layer for Tamm-plasmon-polariton-based organic solar cells

Rashid G. Bikbaev,[1,2,*] Dmitrii A. Pykhtin,[2] Stepan Ya. Vetrov,[1,2] Ivan V. Timofeev,[1,2] and Vasily F. Shabanov[1]

[1]Kirensky Institute of Physics, Federal Research Center KSC SB RAS, Krasnoyarsk 660036, Russia
[2]Siberian Federal University, Krasnoyarsk 660041, Russia
*Corresponding author: bikbaev@iph.krasn.ru

Received 1 March 2022; revised 14 May 2022; accepted 16 May 2022; posted 19 May 2022; published 2 June 2022

The influence of the volume fraction of plasmonic nanoparticles on the efficiency of the Tamm-plasmon-polariton-based organic solar cell is investigated in the framework of temporal coupled mode theory and confirmed by the transfer matrix method. It is shown that, unlike a conventional plasmonic solar cell, in which the efficiency is directly proportional to the volume fraction of nanoparticles in the photosensitive layer, the efficiency of the proposed solar cell reaches the highest value at low volume fractions. This effect is explained by the fact that at these volume fractions, the critical coupling condition of the incident field with the Tamm plasmon polariton is fulfilled. Thus, for the incoming radiation range of 350 to 500 nm, a maximal cell efficiency of 28% is achieved with a volume fraction of nanoparticles equal to 10%. Additionally, the optical properties of the photosensitive layer are compared for the cases of determining its complex refractive index by effective medium theory and the S-parameter retrieval method. A good agreement between the results is demonstrated, which encourages the use of the effective medium theory for preliminary calculations. © 2022 Optica Publishing Group

https://doi.org/10.1364/AO.456413

1. INTRODUCTION

The progress in solar energy goes towards enhancing energy conversion efficiency while simultaneously increasing reliability and decreasing the cost of solar cells. Accordingly, in the last 15 years, conjugated polymer-based organic solar cells (OSCs) have been rapidly developed, which are attractive for their low cost and weight and the mechanical flexibility of solar panels [1–3]. Since such OSCs contain a bulk heterojunction, it is necessary to find a compromise between the photon absorption and carrier transport efficiencies. In this case, the thickness of a photosensitive layer (PSL) is no larger than 100 nm, which significantly limits the efficiency of absorption of incident light. In view of the aforesaid, methods for manipulating light for increasing the absorption in the PSL by means of internal scattering or the plasmon resonance effect have found wide applications. In particular, the authors of [4] experimentally demonstrated the possibility of increasing the absorption of light in a photoactive layer containing silver nanoparticles (Ag NPs). In [5], it was shown that the absorption line of the PSL can be broadened by embedding particles of various shapes into it. The influence of monodisperse Au and Ag NPs on the performance of OSC was investigated in [6]. This direction has gained wide use. The PSL was added with nanowires [7], nanorods [3], particles in the form of cubes, dodecahedra, octahedra, triangular plates [8], and core–shell NPs [9].

Another important way of increasing the integral absorption in the PSL is the introduction of a photonic crystal (PhC) comprising WO_3/LiF [10–12] and TiO_2/SiO_2 [13] layers into an OSC. The high reflectivity in the PhC bandgap ensures the repeated transmission of light incident onto the structure through the PSL, thereby increasing OSC efficiency. Recently, we have proposed to use the PSL doped with plasmonic NPs as a mirror confining a 1D PhC [14]. In this case, a Tamm plasmon polariton (TPP) [15–24] is localized at the PSL–PhC interface, which leads to the occurrence of an additional absorption band of the radiation incident onto the structure and, consequently, increasing the efficiency of the OSC. This structure makes it possible to entirely exclude a metallic contact and thus ensure the absorption mainly in the PSL. In this case, the dispersion of the PSL was determined by the effective medium theory (EMT). In this work, the 2D array of plasmonic NPs embedded in PSL was considered. Importantly, such structures can be obtained by self-assembly, which significantly reduces their cost and speeds up production [25]. The influence of the volume fraction of plasmonic NPs in the PSL absorption of the TPP-based solar cell was examined by the transfer matrix method and coupled mode theory.

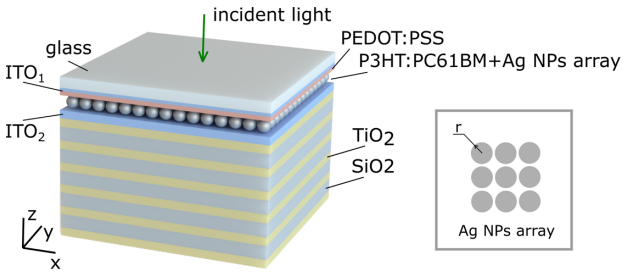

Fig. 1. Schematic of the multilayer solar cell. The photocurrent between indium tin oxide (ITO) contacts is proportional to light absorption in P3HT:PC61BM layer. The critically coupled broadband Tamm plasmon polariton (TPP) at the upper boundary of TiO_2/SiO_2-multilayer concentrates the energy flow by periodically deposited silver nanoparticles.

2. DESCRIPTION OF THE MODEL

A schematic of the investigated cell is shown in Fig. 1(a). The poly (3-hexylthiophene-2,5-diyl): [6,6]-phenyl-C61-butyric acid methyl ester (P3HT:PC61BM) PSL [26] layer thickness is $d_{\mathrm{PSL}} = 70$ nm. The spherical Ag NP radius is $r = 30$ nm. The permittivity of Ag was taken from experimental data [27]. The thickness of the poly(3,4-ethylenedioxythiophene) polystyrene sulfonate (PEDOT:PSS) layer [28] is 20 nm. The transparent contacts used were indium tin oxide (ITO) films with thicknesses of $d_{\mathrm{ITO}_1} = 15$ and $d_{\mathrm{ITO}_2} = 45$ nm. A PhC unit cell was formed from silicon dioxide SiO_2 [29] and titanium dioxide TiO_2 [30] with thicknesses of $d_{\mathrm{SiO}_2} = 61$ nm and $d_{\mathrm{TiO}_2} = 40$ nm, respectively. The number of PhC layers N = 11. The refractive index of semi-infinite optical glass is $n_g = 1.5$.

The effective refractive index of the square array [see Fig. 1(b)] embedded in the PSL was obtained by numerical calculations (S-parameter retrieval method [31,32]). The effective refractive index of the PSL, in this case, can be defined as

$$n_{\mathrm{eff}} = \frac{1}{k d_{\mathrm{PSL}}} \cos^{-1}\left(\frac{1 - S_{11}^2 + S_{21}^2}{2S_{21}}\right), \tag{1}$$

where k is the wave vector, and S_{11} and S_{21} are the components of the scattering matrix.

It is noteworthy that this method makes it possible to determine the effective parameters of films with an arbitrarily large volume fraction of NPs. The dependences of the real and imaginary parts of the effective refractive index of the PSL with the square array for different volume fractions of Ag NPs are shown in Fig. 2.

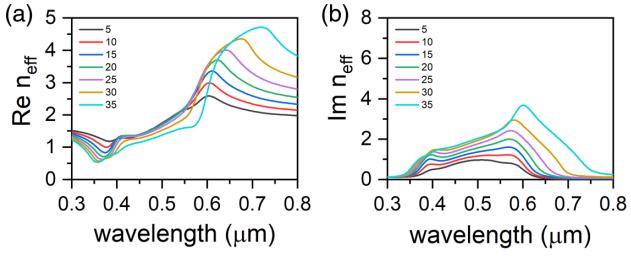

Fig. 2. S-parameter retrieval method, Eq. (1), is used to determine (a) real Re n_{eff} and (b) imaginary Im n_{eff} parts of the effective refractive index of a square array of silver nanoparticles for different volume fractions f (in %).

It can be seen from the figure that increasing the volume fraction increases the optical response of the medium, which manifests itself in the form of a resonance near 600 nm.

3. RESULTS AND DISCUSSION

A. Coupled Mode Theory

According to temporal coupled mode theory [33,34], any state (resonance) has its own frequency ω_0 and number N of energy channels outside and inside the resonance. In this case, the energy loss in the channels is described by the relaxation times τ_l or relaxation rates $\gamma_l = 1/\tau_l$, where $l = 1, 2, \ldots, N$. If the energy leaves the state along two energy channels with relaxation times τ_1 and τ_2, then the relaxation time of the state is determined as $1/\tau = 1/\tau_1 + 1/\tau_2$. In the presented solar cell, three energy channels contribute to TPP formation. We denote the energy relaxation to PSL transmission, absorption, and PhC transmission channels as γ_{PSL}, γ_{A}, and γ_{PhC}, respectively. Each channel relaxation rate is proportional to its power flow divided by the energy accumulated in the TPP. So, the relaxation rates are related to corresponding energy coefficients of the structure as [35]

$$\gamma_{\mathrm{PSL}} : \gamma_{\mathrm{A}} : \gamma_{\mathrm{PhC}} = T_{\mathrm{PSL}} : A_{\mathrm{PSL}} : T_{\mathrm{PhC}}. \tag{2}$$

In the case of opaque PhC, its relaxation channel can be ignored ($\gamma_{\mathrm{PhC}} = 0$). As a result, the critical coupling condition (2) can be written in the form

$$\gamma_{\mathrm{PSL}} = \gamma_{\mathrm{A}}; \quad \gamma_{\mathrm{PhC}} = 0 \Leftrightarrow T_{\mathrm{PSL}} = A_{\mathrm{PSL}}; \quad T_{\mathrm{PhC}} = 0. \tag{3}$$

This equation can be solved graphically. To do this, we should build the parametric dependence $A_{\mathrm{PSL}}(T_{\mathrm{PSL}})$. We consider the PSL film with refractive index n_{eff}, which is located between ITO and PEDOT layers with refractive indices n_{ITO} and n_{PEDOT}. The transmittance, reflectance, and absorptance of the PSL film are determined using the Airy formulas

$$T_{\mathrm{PSL}} = \frac{n_{\mathrm{PEDOT}}}{n_{\mathrm{ITO}}}\left|\frac{t_{12} + t_{23}e^{i\beta}}{1 + r_{12}r_{23}e^{2i\beta}}\right|^2, \quad R_{\mathrm{PSL}} = \left|\frac{r_{12} + r_{23}e^{2i\beta}}{1 + r_{12}r_{23}e^{2i\beta}}\right|^2,$$

$$A_{\mathrm{PSL}} = 1 - T_{\mathrm{PSL}} - R_{\mathrm{PSL}}, \tag{4}$$

where $\beta = 2\pi n_{\mathrm{eff}} d_{\mathrm{PSL}}/\lambda$ is the phase incoming during the passage of the layer by the wave; λ is the wavelength; d_{PSL} is the PSL film thickness $t_{12} = 2n_{\mathrm{ITO}}/(n_{\mathrm{ITO}} + n_{\mathrm{eff}})$, $r_{12} = (n_{\mathrm{ITO}} - n_{\mathrm{eff}})/(n_{\mathrm{ITO}} + n_{\mathrm{eff}})$ and $t_{23} = 2n_{\mathrm{eff}}/(n_{\mathrm{eff}} + n_{\mathrm{PEDOT}})$, $r_{23} = (n_{\mathrm{eff}} - n_{\mathrm{PEDOT}})/(n_{\mathrm{eff}} + n_{\mathrm{PEDOT}})$ are the amplitudes of transmission and reflection at interfaces 1–2 and 2–3.

Figure 3 presents rather simplified calculations of the critical coupling condition of the incident field to the TPP for various volume fractions from 5% to 30%. In other words, at these concentrations, the highest resonant (non-integral) absorption in the PSL layer is achieved. For a larger volume fraction, the $A(T)$ curve does not intersect the critical coupling dashed line, because an increase in the concentration from 5% to 30% leads to a shift of the critical coupling wavelength λ_{CC} to the short-wave edge of the PhC stop band. Thus, to ensure the highest integral absorption in the PSL, it is necessary to blueshift the stop band by reducing the PhC period.

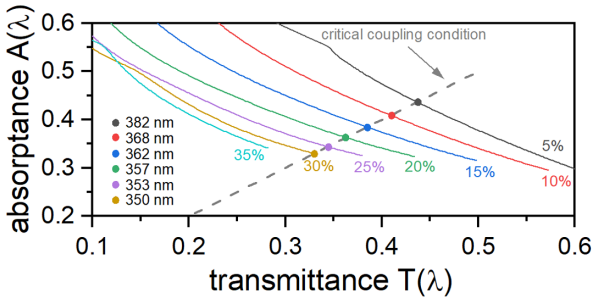

Fig. 3. Absorptance $A(\lambda)$ of the PSL film increases while its transmittance $T(\lambda)$ decreases in range of 350 to 500 nm for various volume fractions f (solid curves). The critical coupling (CC) condition [Eq. (3)] is shown by a dashed strait line. The graphical solution is at the intersection of the dashed line with each solid curve represented by six filled circles. Corresponding wavelengths λ_{CC} are presented. The PSL film thickness is $d_{PSL} = 70$ nm.

B. Transfer Matrix Simulation

Here we accurately verify the graphical parameter optimization presented in Fig. 3. With this purpose in mind, we recalculate the integral absorption of the PSL layer by the transfer matrix method [36]. The integral absorption is meant to be the PSL absorption normalized to the solar radiation spectrum. Generally, the integral absorption is determined for each of two polarizations, A_{TE} and A_{TM}, separately, and their arithmetic mean $A_{total} = (A_{TE} + A_{TM})/2$ yields the total absorption in the layer. At normal incidence, we have $A_{total} = A_{TE} = A_{TM}$, which can be determined as

$$A_{total} = \frac{\int_{\lambda_1}^{\lambda_2} A(\lambda) S(\lambda) d\lambda}{\int_{\lambda_1}^{\lambda_2} S(\lambda) d\lambda}, \tag{5}$$

where $\lambda_1 = 350$ nm, $\lambda_2 = 500$ nm, $A(\lambda)$ is the absorption in the PSL, and $S(\lambda)$ is the solar radiation spectrum (AM1.5). In this paper, we do not separate absorption in the Ag NPs or in the P3HT:PC61BM material. This is due to the fact that by homogenizing the active layer doped with plasmonic NPs, we obtain a medium with effective parameters. In the wavelength range of 350 to 500 nm, we assume the NP absorption is smaller than P3HT:PC61BM absorption [Fig. 2(b)]. Moreover, the NP absorption is also useful because it leads to the injection of hot electrons and, consequently, to an increase in photocurrent [37,38].

The conjugation of the PSL containing an embedded square plasmonic array with the PhC will lead to the formation of a TPP at their interface; at the wavelength of the TPP, the integral absorption in the PSL, the wavelength of which is dictated by the phase matching condition [15,39,40], will increase. This condition can be met by changing the thickness of the ITO_2 film adjacent to the PhC [please see Fig. 4(a)].

It can be seen that the highest integrated absorption in the PSL is obtained at an ITO_2 film thickness of 30 nm and $f = 10\%$. The integrated absorption in the PSL in this case equals 90%. Corresponding absorptance spectra of the PSL layer are shown in Fig. 4(b). The increase in integrated absorption is induced by the excitation of a TPP localized at the interface between the PhC and the active layer doped with plasmonic NPs. This is also confirmed by the spatial field distribution.

In Fig. 5(a), the field is localized at the PhC–PSL interface and decays exponentially on both sides of it. This slight increase in the field at the TPP wavelength for the square array is explained by the low Q factor of the TPP [40].

In Fig. 5(b), the reflectance spectra of the structure show that critical coupling is not observed for all $f = 5-30\%$, as predicted by the coupled mode theory, but for $f = 10-20\%$ only. It should be clarified that the coupled mode theory quantitatively describes only high-Q resonances, while for low-Q resonances, it gives only a qualitative picture. Nevertheless, for both methods, the results are in good agreement.

C. Effective Medium Theory versus S-Parameter Retrieval Method

At low concentrations of Ag NPs in the bulk of the PSL ($0.01 < f < 0.3$ [41]), the permittivity of the P3HT:PC61BM layer doped by Ag NPs can be determined by the Maxwell–Garnett model [42]:

$$\varepsilon_{eff} = \varepsilon_d(\omega)\left[1 + \frac{f(\varepsilon_m(\omega) - \varepsilon_d(\omega))}{\varepsilon_d(\omega) + (1-f)(\varepsilon_m(\omega) - \varepsilon_d(\omega))/3}\right], \tag{6}$$

where f is the volume fraction; $\varepsilon_d(\omega)$ [26] and $\varepsilon_m(\omega)$ are dielectric permittivity of the matrix (P3HT:PC61BM) and Ag NPs, respectively; ω is radiation frequency. Figure 6 illustrates a comparison of the integrated absorption spectra of the structure for various methods of determining the effective dielectric permittivity of the PSL. Simulations were performed for volume fractions lying in the range of 5% to 20%.

Moreover, when determining the effective refractive index of the PSL layer by the EMT method, the dispersion of metal NPs was taken into account in two different ways. First, the permittivity was given by the Drude model ($\hbar\omega_p = 9$ eV, $\hbar\gamma = 0.02$ eV, $\varepsilon_0 = 5$), and then from the *Handbook of Optical Constants of Solids* [43]. The permittivities of the PSL are denoted as $\varepsilon_{MG-Drude}$ and ε_{MG-CRC}, respectively. A comparison of the spectra showed that all three results have good agreement only at low volume fractions [see Fig. 6(a)]. An increase in the volume fraction of NPs leads to the fact that the results obtained using the Maxwell–Garnett model with the Drude relation increasingly deviate from the results obtained by S-parameter retrieval. At the same time, a more correct accounting of the NP dispersion allows us to obtain a good agreement between the

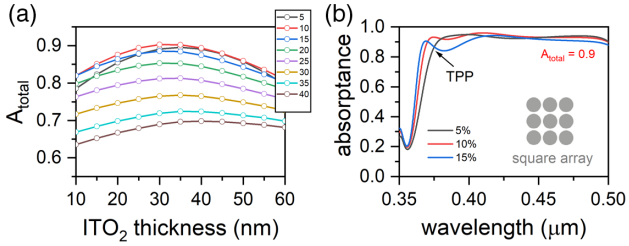

Fig. 4. (a) Total integrated absorption in PSL versus ITO layer thickness for various volume fractions f (in %); (b) absorptance spectra of PSLs for $d_{PSL} = 70$ nm and $d_{ITO_2} = 30$ nm were obtained by the S-parameter retrieval method for different volume fractions f.

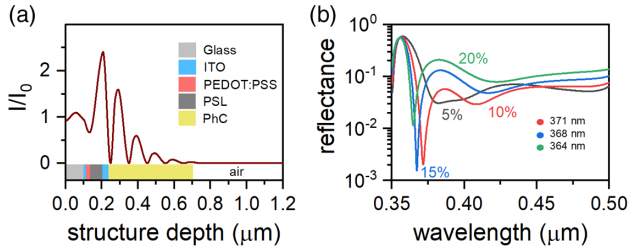

Fig. 5. (a) Local field intensity $|E|^2$ spatial distribution at the TPP wavelength and (b) reflectance spectra of the structure for various volume fractions f.

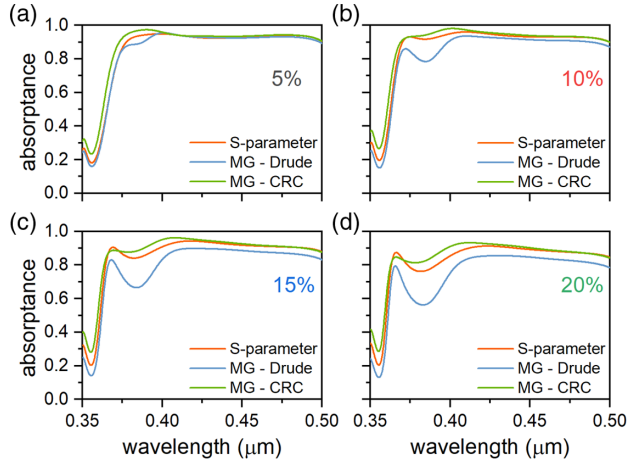

Fig. 6. Integral absorption of a photosensitive layer in the case of determining its effective permittivity by S-parameter retrieval and EMT methods for (a) $f = 5\%$, (b) $f = 10\%$, (c) $f = 15\%$, and (d) $f = 20\%$.

EMT and the direct numerical calculation up to the volume fraction $f = 20\%$ [see Figs. 6(b)–6(d)].

D. Detailed Balance Analysis of Tamm-Plasmon-Polariton-Based Solar Cells

The detailed balance equation [44,45] for the OSC has the form

$$F_s - F_c(V) - R(V) - J/q = 0, \tag{7}$$

where V is the voltage across the cell, J is the total current density, q is the elementary charge, F_s is the radiative generation of hole–electron pairs by incident sunlight, $F_c(V)$ is the radiative recombination, and $R(V)$ is the non-radiative recombination of hole–electron pairs. The radiative generation F_s can be calculated as

$$F_s = \frac{1}{hc}\int_{\lambda_1}^{\lambda_2} \lambda S(\lambda) A(\lambda) \mathrm{d}\lambda. \tag{8}$$

The radiative recombination $F_c(V)$ relates to the voltage V as

$$F_c(V) = F_{co} e^{\frac{qV}{kT}} = e^{\frac{qV}{kT}} \int_{\lambda_1}^{\lambda_2} \Theta(\lambda) A(\lambda) \mathrm{d}\lambda, \tag{9}$$

where $\Theta(\lambda) = \frac{2c}{\lambda^4}[e^{hc/\lambda kT} - 1]^{-1}$ is the Plank law, k is the Boltzman constant, T is the temperature of the cell, h is the Plank constant, and c is the speed of light.

The short-circuit current J_{sc} is determined from Eq. (7) by equating V to zero:

$$J_{sc} = q(F_s - F_c(0)). \tag{10}$$

On the other hand, open-circuit voltage V_{oc} across the cell can be obtained from Eq. (7) by setting $J = 0$:

$$F_s = F_c(V_{oc}) + R(V_{oc}). \tag{11}$$

In the case when the contribution of non-radiative processes is small, V_{oc} can be approximated as

$$V_{oc} \approx \frac{kT}{q} \ln\left(\frac{F_s}{F_{co}}\right). \tag{12}$$

For solar cell efficiency, the non-radiative recombination mechanisms are of crucial importance. There are three types of recombination: Auger recombination, the defect mediated Shockley–Read–Hall effect, and surface recombination. In an effort to obtain the highest performance of a solar cell, we idealize the case of a defect-free solar cell with an ideal passivation of the surface. In this case, the only unconventional mechanism in our detailed balance analysis is Auger recombination, which can be define as follows:

$$R(V)_{\mathrm{Auger}} = 2C d_{\mathrm{PSL}} n_i^2 e^{\frac{3qV}{2kT}}, \tag{13}$$

where $C = 2.7 \cdot 10^{-30}$ $(\mathrm{cm}^6/\mathrm{s})$ is the Auger coefficient [46], and $n_i = 9.62 \cdot 10^8$ (cm^{-3}) is the intrinsic carrier concentration.

The efficiency of the solar cell was calculated by the equation [44,45]

$$\eta = \frac{V_{oc} J_{sc} FF}{P_{inc}} \times 100\%, \tag{14}$$

where FF is the fill factor of the solar cell, and P_{inc} is the power of incident light. FF is a parameter that, in conjunction with V_{oc} and J_{sc}, determines the maximum power from a solar cell. FF is defined as the ratio of the maximum power from the solar cell to the product of V_{oc} and J_{sc} so that

$$\mathrm{FF} = \frac{J_{mp} V_{mp}}{J_{sc} V_{oc}}, \tag{15}$$

where J_{mp} and V_{mp} are current and voltage at the maximal power point of the solar cell, respectively. In our simulation, $\mathrm{FF} \approx 0.41$, and $P_{inc} \approx 171.9$ $(\mathrm{W/m^2})$.

The simulation results are shown in Fig. 7. The surface current density and efficiency of the solar cells were calculated within the PhC bandgap. This is due to the excitation of the TPP. Moreover, the calculation of integral absorption in a wide range of wavelengths outside the PhC bandgap is not quite correct. This is due to the fact that plasmon resonance appears near 600 nm, near which most of the incident radiation will be absorbed in NPs and not in the PSL.

For the highest integral absorption ($f = 10\%$), the surface current density is $J = 55.2$ $(\mathrm{A/m^2})$. An increase in the volume concentration, in accordance with the previously performed calculations, leads to a smooth decrease in the current density [see Fig. 7(a)]. At the same time, the efficiency of the proposed solar cell in the same concentration range drops from 27.8%

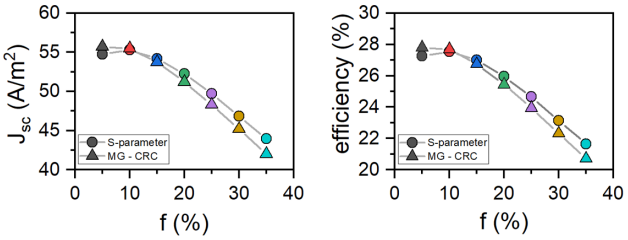

Fig. 7. (a) J_{sc} and (b) efficiency of the solar cell for different values f.

to 21.6%. Moreover, we compared the surface current density and the efficiency of the solar cell in the case of determining the effective dielectric permittivity of the PSL by S-parameters and the EMT. When using the EMT, the surface current density and efficiency of the solar cell are slightly smaller. The difference on average is no more than 2%. Thus, the effective medium model can be used to describe the optical properties of the device with an accuracy not inferior to that of direct numerical calculations. It should be noted that the efficiency of the proposed solar cell can be increased by further broadening [40] the TPP spectral line or by hybridizing the TPP with other types of localized modes [47].

4. CONCLUSION

The spectral properties of a model of an OSC based on a TPP localized at the interface between a PhC and a PSL with an embedded square plasmon array were studied. The effective refractive index of the PSL was determined by the S-parameter retrieval method; the energy spectra of the structure and its local intensity distribution were calculated by the transfer matrix method. The influence of the volume fraction of NPs in the active layer on the spectral properties of the solar cell was studied. It is shown that the greatest integral absorption and efficiency are provided only at small volume fractions. This is explained by the fact that at these volume fractions, the critical coupling condition of the incident field with the TPP is fulfilled. A comparative computation of the integral absorption in the PSL with optical properties determined using the EMT and direct numerical calculation was made. It was shown that, at low (about 20%) concentrations of NPs in the bulk of the PSL, the results obtained by two different methods agree well. Thus, the MG model can be used at the first (estimation) stages of the calculation of the optical properties of such structures with an accuracy comparable to that of direct calculation.

Funding. Council on Grants of the President of the Russian Federation (MK-46.2021.1.2).

Disclosures. The authors declare no conflicts of interest.

Data availability. Data underlying the results presented in this paper are not publicly available at this time but may be obtained from the authors upon reasonable request.

REFERENCES

1. H. Atwater and A. Polman, "Plasmonics for improved photovoltaic devices," Nat. Mater. **9**, 205–213 (2010).
2. A. Heeger, "25th anniversary article: Bulk heterojunction solar cells: understanding the mechanism of operation," Adv. Mater. **26**, 10–28 (2014).
3. Z. He, B. Xiao, F. Liu, H. Wu, Y. Yang, S. Xiao, C. Wang, T. Russell, and Y. Cao, "Single-junction polymer solar cells with high efficiency and photovoltage," Nat. Photonics **9**, 174–179 (2015).
4. D. Duche, P. Torchio, L. Escoubas, F. Monestier, J.-J. Simon, F. Flory, and G. Mathian, "Improving light absorption in organic solar cells by plasmonic contribution," Sol. Energy Mater. Sol. Cells **93**, 1377–1382 (2009).
5. X. Li, W. C. H. Choy, H. Lu, W. E. I. Sha, and A. H. P. Ho, "Efficiency enhancement of organic solar cells by using shape-dependent broadband plasmonic absorption in metallic nanoparticles," Adv. Funct. Mater. **23**, 2728–2735 (2013).
6. H. Kacus, O. Metin, M. Sevim, M. Biber, A. Baltakesmez, and S. Aydogan, "A comparative study on the effect of monodisperse Au and Ag nanoparticles on the performance of organic photovoltaic devices," Opt. Mater. **116**, 111082 (2021).
7. C.-H. Kim, S.-H. Cha, S. Chul Kim, M. Song, J. Lee, W. Suk Shin, S.-J. Moon, J. Hwan Bahng, N. A. Kotov, and S.-H. Jin, "Silver nanowire embedded in P3HT:PCBM for high-efficiency hybrid photovoltaic device applications," ACS Nano **5**, 3319–3325 (2011).
8. W.-H. Tseng, C.-Y. Chiu, S.-W. Chou, H.-C. Chen, M.-L. Tsai, Y.-C. Kuo, D.-H. Lien, Y.-C. Tsao, K.-Y. Huang, C.-T. Yeh, J.-H. He, C.-I. Wu, M. H. Huang, and P.-T. Chou, "Shape-dependent light harvesting of 3D gold nanocrystals on bulk heterojunction solar cells: plasmonic or optical scattering effect?" J. Phys. Chem. C **119**, 7554–7564 (2015).
9. W. B. Chen, L. Y. Hu, F. Meng, L. Tang, S. Liang, and J. B. Li, "Dual-plasmon-induced photocatalytic performance enhancement in Au-PbS-CdS nanodumbbells with double Au caps on the ends," Opt. Mater. **117**, 111210 (2021).
10. W. Yu, L. Shen, Y. Long, W. Guo, F. Meng, S. Ruan, X. Jia, H. Ma, and W. Chen, "Semitransparent polymer solar cells with one-dimensional $(wo^3/lif)^n$ photonic crystals," Appl. Phys. Lett. **101**, 153307 (2012).
11. W. Yu, L. Shen, P. Shen, F. Meng, Y. Long, Y. Wang, T. Lv, S. Ruan, and G. Chen, "Simultaneous improvement in efficiency and transmittance of low bandgap semitransparent polymer solar cells with one-dimensional photonic crystals," Sol. Energy Mater. Sol. Cells **117**, 198–202 (2013).
12. W. Yu, S. Ruan, Y. Long, L. Shen, W. Guo, and W. Chen, "Light harvesting enhancement toward low IPCE region of semitransparent polymer solar cells via one-dimensional photonic crystal reflectors," Sol. Energy Mater. Sol. Cells **127**, 27–32 (2014).
13. R. R. Lunt and V. Bulovic, "Transparent, near-infrared organic photovoltaic solar cells for window and energy-scavenging applications," Appl. Phys. Lett. **98**, 113305 (2011).
14. R. G. Bikbaev, S. Y. Vetrov, I. V. Timofeev, and V. F. Shabanov, "Photosensitivity and reflectivity of the active layer in a Tamm-plasmon-polariton-based organic solar cell," Appl. Opt. **60**, 3338–3343 (2021).
15. M. Kaliteevski, I. Iorsh, S. Brand, R. A. Abram, J. M. Chamberlain, A. V. Kavokin, and I. A. Shelykh, "Tamm plasmon-polaritons: possible electromagnetic states at the interface of a metal and a dielectric Bragg mirror," Phys. Rev. B **76**, 165415 (2007).
16. M. E. Sasin, R. P. Seisyan, M. Kaliteevski, S. Brand, R. A. Abram, J. M. Chamberlain, A. Y. Egorov, A. P. Vasil'ev, V. S. Mikhrin, and A. V. Kavokin, "Tamm plasmon polaritons: Slow and spatially compact light," Appl. Phys. Lett. **92**, 251112 (2008).
17. S. Y. Vetrov, R. G. Bikbaev, and I. Timofeev, "Optical Tamm states at the interface between a photonic crystal and a nanocomposite with resonance dispersion," J. Exp. Theor. Phys. **117**, 988–998 (2013).
18. S. Y. Vetrov, R. G. Bikbaev, and I. Timofeev, "The optical Tamm states at the edges of a photonic crystal bounded by one or two layers of a strongly anisotropic nanocomposite," Opt. Commun. **395**, 275–281 (2017).
19. R. Bikbaev, S. Vetrov, and I. Timofeev, "Epsilon-near-zero absorber by Tamm plasmon polariton," Photonics **6**, 28 (2019).
20. F. Wu, X. Wu, S. Xiao, G. Liu, and H. Li, "Broadband wide-angle multilayer absorber based on a broadband omnidirectional optical Tamm state," Opt. Express **29**, 23976–23987 (2021).

21. C.-H. Xue, F. Wu, H.-T. Jiang, Y. Li, Y.-W. Zhang, and H. Chen, "Wide-angle spectrally selective perfect absorber by utilizing dispersionless Tamm plasmon polaritons," Sci. Rep. **6**, 39418 (2016).
22. J. Hu, Y. Huang, Y. Chen, Z. da Hu, J. Wu, and J. Wang, "High-sensitivity multi-channel refractive-index sensor based on a graphene-based hybrid Tamm plasmonic structure," Opt. Mater. Express **11**, 3833–3843 (2021).
23. J. Hu, M. Li, Z. Wang, Z. Hu, J. Wang, S. Khakhomov, and I. Semchenko, "High-performance terahertz refractive index sensor based on a hybrid graphene Tamm structure," J. Opt. Soc. Am. B **38**, 2543–2550 (2021).
24. J. Hu, Z. Hu, J. Wang, A. Balmakou, S. Khakhomov, and I. Semchenko, "High-performance tunable multichannel absorbers coupled with graphene-based grating and dual-Tamm plasmonic structures," Plasmonics **17**, 287–294 (2021).
25. J.-H. Huh, J. Lee, and S. Lee, "Soft plasmonic assemblies exhibiting unnaturally high refractive index," Nano Lett. **20**, 4768–4774 (2020).
26. C. Stelling, C. R. Singh, M. Karg, T. A. F. König, M. Thelakkat, and M. Retsch, "Plasmonic nanomeshes: their ambivalent role as transparent electrodes in organic solar cells," Sci. Rep. **7**, 42530 (2017).
27. D. Lide, *CRC Handbook of Chemistry and Physics: A Ready-Reference Book of Chemical and Physical Data* (CRC Press, 1995).
28. C.-W. Chen, S.-Y. Hsiao, C.-Y. Chen, H.-W. Kang, Z.-Y. Huang, and H.-W. Lin, "Optical properties of organometal halide perovskite thin films and general device structure design rules for perovskite single and tandem solar cells," J. Mater. Chem. A **3**, 9152–9159 (2015).
29. I. H. Malitson, "Interspecimen comparison of the refractive index of fused silica," J. Opt. Soc. Am. **55**, 1205–1209 (1965).
30. J. R. DeVore, "Refractive indices of rutile and sphalerite," J. Opt. Soc. Am. **41**, 416–419 (1951).
31. D. R. Smith, D. C. Vier, T. Koschny, and C. M. Soukoulis, "Electromagnetic parameter retrieval from inhomogeneous metamaterials," Phys. Rev. E **71**, 036617 (2005).
32. S. Mehrabi, M. H. Rezaei, and M. R. Rastegari, "High-efficient plasmonic solar absorber and thermal emitter from ultraviolet to near-infrared region," Opt. Laser Technol. **143**, 107323 (2021).
33. H. Haus, *Waves and Fields in Optoelectronics* (Prentice-Hall, 1984).
34. J. D. Joannopoulos, S. G. Johnson, J. N. Winn, and R. D. Meade, *Photonic Crystals : Molding the Flow of Light* (Princeton University, 2008).
35. Z.-Y. Yang, S. Ishii, T. Yokoyama, T. D. Dao, M.-G. Sun, P. S. Pankin, I. Timofeev, T. Nagao, and K.-P. Chen, "Narrowband wavelength selective thermal emitters by confined Tamm plasmon polaritons," ACS Photon. **4**, 2212–2219 (2017).
36. P. Yeh, "Electromagnetic propagation in birefringent layered media," J. Opt. Soc. Am. **69**, 742–756 (1979).
37. L. Chen, S. Mao, P. Wang, Z. Yao, Z. Du, Z. Zhu, L. A. Belfiore, and J. Tang, "Visible light driven hot-electron injection by pd nanoparticles: fast response in metal–semiconductor photodetection," Adv. Opt. Mater. **9**, 2001505 (2020).
38. D. Lee, S. G. Han, J. Mun, K. Yang, S. H. Kim, J. Rho, K. Cho, D. X. Oh, and M. S. Jeong, "Elucidating the photoluminescence-enhancement mechanism in a push-pull conjugated polymer induced by hot-electron injection from gold nanoparticles," Photon. Res. **9**, 131–141 (2021).
39. F. Wu, J. Wu, C. Fan, Z. Guo, C. Xue, H. Jiang, Y. Sun, Y. Li, and H. Chen, "Omnidirectional optical filtering based on two kinds of photonic band gaps with different angle-dependent properties," Europhys. Lett. **129**, 34004 (2020).
40. A. M. Vyunishev, R. G. Bikbaev, S. E. Svyakhovskiy, I. V. Timofeev, P. S. Pankin, S. A. Evlashin, S. Y. Vetrov, S. A. Myslivets, and V. G. Arkhipkin, "Broadband Tamm plasmon polariton," J. Opt. Soc. Am. B **36**, 2299–2305 (2019).
41. J. E. Spanier and I. P. Herman, "Use of hybrid phenomenological and statistical effective-medium theories of dielectric functions to model the infrared reflectance of porous SiC films," Phys. Rev. B **61**, 10437–10450 (2000).
42. J. C. Maxwell-Garnett, "Colours in metal glasses, in metallic films, and in metallic solutions. II," Philos. Trans. R. Soc. A **205**, 237–288 (1906).
43. E. D. Palik, ed., "Front matter," in *Handbook of Optical Constants of Solids* (Academic, 1998), p. iii.
44. K. Kim and S. Lee, "Detailed balance analysis of plasmonic metamaterial perovskite solar cells," Opt. Express **27**, A1241–A1260 (2019).
45. S. Sandhu, Z. Yu, and S. Fan, "Detailed balance analysis of nanophotonic solar cells," Opt. Express **21**, 1209–1217 (2013).
46. T. Kirchartz, B. E. Pieters, J. Kirkpatrick, U. Rau, and J. Nelson, "Recombination via tail states in polythiophene:fullerene solar cells," Phys. Rev. B **83**, 115209 (2011).
47. B. I. Afinogenov, V. O. Bessonov, A. A. Nikulin, and A. A. Fedyanin, "Observation of hybrid state of Tamm and surface plasmon-polaritons in one-dimensional photonic crystals," Appl. Phys. Lett. **103**, 061112 (2013).